

Screening response of valence and core electrons in a metal: Inelastic x-ray scattering study

N. Hiraoka^{1,*}, T. Hagiya^{2,†} and K. Matsuda³

¹*National Synchrotron Radiation Research Center, Hsinchu 30076, Taiwan*

²*Graduate School of Science, Kyoto University, Kyoto 606-8502, Japan*

³*Graduate School of Science, Kumamoto University, Kumamoto 860-8555, Japan*

 (Received 12 June 2022; revised 18 August 2023; accepted 29 September 2023; published 2 November 2023)

The screening response of valence and core electrons against a test charge embedded in a metal is investigated. The real space-and-time dynamical response function $\chi(r, t)$ is derived from the x-ray inelastic scattering spectra measured over a wide momentum and energy space on elementary Li. Embedding a charge initially induces local screening due to core electrons. This is followed by screening due to valence electrons, which exhibits an oscillatory behavior where the frequency is determined by the plasmon energy. Finally, static screening charges are produced. The static screening charge consists of a local electron cloud surrounding the embedded charge over several angstroms and the oscillatory charge densities have a periodicity twice that of the Fermi wave number in a larger r scale (i.e., the Friedel oscillation). The core electrons also exhibit an oscillatory behavior, where the frequency is determined by the absorption edge energy. This eventually leads to more local screening, further reducing the screening distance.

DOI: [10.1103/PhysRevB.108.195104](https://doi.org/10.1103/PhysRevB.108.195104)

I. INTRODUCTION

A fundamental and critical problem in condensed matter physics is the screening effect. An external potential perturbs electron gas. This redistributes the electrons, creating an additional Coulomb potential. Consequently, the potential probed by a test charge differs from the external one. The screening effect is basically a many-body problem, which cannot be exactly solved in many cases. To overcome the problem, various types of the approximations such as the density functional theory (for ground states) and the time-dependent density functional theory (excited states) [1–4] or numerical diagonalizations on finite size systems such as quantum Monte Carlo simulations [5–7] have been developed. One of the most simple and familiar examples of the screening effect in real matter is the effective ionic potential in a metal. Conduction electrons aggregate near ions to screen positive charges. Hence the effective potential felt by a test charge becomes much more attenuated than the bare one. Another type of screening effect is the so-called Friedel oscillation, which reaches a rather long distance. It exhibits an oscillatory behavior in real space at a periodicity twice that of the Fermi wave number.

Screening effects in an electron gas are expressed by a key quantity—the density-density response function of electrons. This plays a crucial role in describing the effective interactions between electron–electron, electron–test charge, and test charge–test charge. Other phenomena such as the collective modes, which are observed in the energy loss scattering process, are also connected with the density-density response function in a unified manner [8,9]. Recently, the

effective interaction in the electron liquid and the screening effects has been theoretically investigated [10–15]. Extended theories have been constructed to evaluate the density response function with the refinement of a local field factor [6] or the inclusion of nonlinear effects [16,17]. The spatial modulation of the local density of states (DOS) has been experimentally observed as the fingerprint of the Friedel oscillation [18–21]. Several studies have attempted to extract information about the Friedel oscillation by evaluating the effective interionic potential in the liquid state based on the integral equation theory. This approach is somewhat empirical because experimental structure factors are used as the input parameters in the calculation [22,23].

The screening effect has been extensively studied but there are few reports for the time dependence. The screening due to the electrons occurs in a timescale of 10–100 attoseconds [24,25]. Typical experiments for such ultrafast phenomena are the pump-probe measurements using a short-pulse laser [26–30]. The advanced laser technology makes the femtosecond or even attosecond spectroscopy possible with the interferometry methods [31,32]. Nevertheless, the typically available energy for photons is <100 eV at present. This fact hampers the access to the density-density response function in the wide momentum range and thus limits a spatial resolution in the Fourier transformation.

Previously we showed that the static response function $\chi(q, \omega \rightarrow 0)$ and the screening charge density $n(r, t \rightarrow \infty)$ are available from the dynamical structure factor, $S(q, \omega)$ [33]. $S(q, \omega)$ is an observable quantity by inelastic x-ray scattering. Here, q and ω represent the wave number and the angular frequency, respectively. Additionally, r is the distance from the test charge and t is the duration time after it is embedded. However, several questions remain unanswered. (i) How is the screening charge induced after the charge is embedded?

*hiraoka@spring8.or.jp

†Present address: Sanyo Special Steel Co Ltd.

That is, what is the time dependence of the screening charge density? (ii) How do the core or bound electrons contribute to screening? Both the valence and core electrons have characteristic features in $S(q, \omega)$. For the Li metal, the former has a plasmon peak observable at low momenta, while the latter shows an absorption edge like feature enhanced at middle or high momenta (although this exists at any momenta), which appear at 7 eV and 60 eV, respectively [34–36]. This study focuses on the dynamical response and discusses how the screening charge evolves over time at an attosecond time resolution (1.03 as).

II. EXPERIMENTS

The experiments were performed on the Taiwan IXS beamline at SPring-8 (BL12XU). Synchrotron radiation from an undulator light source was monochromatized by Si111 double crystals at $E_o = 20$ or 26 keV (more precisely, 19.98 or 25.91 keV, respectively). For the $E_o = 20$ keV experiment, a high-resolution monochromator consisting of a pair of Si220 channel-cut crystals was installed after the Si 111 monochromator to achieve a higher ω resolution (1.2–1.4 eV). For the $E_o = 26$ keV experiment, the spectra was collected at a 5–6 eV resolution without the channel-cut crystals. X rays scattered from the sample were monochromatized by a curved Si analyzer crystal before being counted by a NaI scintillation detector [37]. With a Si 660 reflection, the inelastic spectra were measured in $E_o - E \leq 350$ eV, where $E_o = 19.98$ keV, at 19 points in $q \leq 3.47 \text{ \AA}^{-1}$ (SET-I), while, in $E_o - E \leq 2000$ eV, where $E_o = 25.91$ keV, at 30 points in $q \leq 16.0 \text{ \AA}^{-1}$ (SET-II). Here E represents the scattered photon energy. The samples were elementary Li metal having a thickness of 3 or 10 mm, which were sealed in a cell with He atmosphere. The measurement was performed at room temperature. The count rate in the 20 keV experiment was 1600 counts/s at the plasmon peak when $q = 1.0 \text{ \AA}^{-1}$, while that in the 26 keV experiment was 5500 counts/s at the same peak when $q = 1.15 \text{ \AA}^{-1}$. The counts were accumulated for 10 or 2 s each point. The data were first corrected for the beam intensity variation, the absorption in the samples, and the polarization factor between two wave vectors for the incident and the scattered photons. After the removal of a tail of the elastic line for each spectra, low- q data were fit to the f -sum rule, so that a common normalization factor was determined to obtain $S(q, \omega)$ in an absolute scale. For the high- q data, the f -sum rule was utilized again to find a common normalization factor, but it was only applied at the highest q , 16.0 \AA^{-1} . Finally, two data sets were obtained as shown in Table I: SET-I is the high resolution data, while SET-II is the wide range data in $q - \omega$ space, which provide the wide-range information and the high-resolution information in $r - t$ space, respectively. SET-I is the data identical with ones in the previous report [33], while SET-II is new data [see Fig. 1(a)]. As q increases, $S(q, \omega)$ rather quickly converges to Compton profiles shown in the earlier reports [38,39].

III. MODELS

For a comparison with the experiments, we calculated $S(q, \omega)$ based on two models. One was the electron gas

TABLE I. Obtained data sets in the experiments: SET-I is high resolution data, while SET-II is wide range data in $q - \omega$ space. Those sets inversely provide wide range and high resolution information in $r - t$ space, respectively.

	SET-I	SET-II
ω range	2.0–350 eV	5.0–2000 eV
ω step ($\Delta\omega$)	0.5/1.0 eV	2.5 eV
ω resolution ($\delta\omega$)	1.2–1.4 eV	5–6 eV
q range	0.30–3.5 \AA^{-1}	0.5–16.0 \AA^{-1}
q step (Δq)	0.1/0.2 \AA^{-1}	$\sim 0.5 \text{ \AA}^{-1}$
q resolution (δq)	0.18 \AA^{-1}	0.22 \AA^{-1}
T maximum	4135 (2067) as	827 as
T resolution	5.91 as	1.03 as
r maximum	31.4 (15.7) \AA	6.28 \AA
r resolution	0.90 \AA	0.20 \AA

model based on random phase approximation (RPA). $S(q, \omega)$ was calculated from a Lindhard dielectric function $\epsilon_L(q, \omega)$ (see, e.g., Ref. [40]) for Fermi momentum $k_F = 1.112 \text{ \AA}^{-1}$. $\epsilon_L(q, \omega)$ was convoluted with the Lorentzian having a 2 eV width before calculating $S(q, \omega)$, so that the plasmon has a finite lifetime broadening. The range and the step were 350 and 0.5 eV, respectively. In order to compare the RPA model with the experiment over a wide $q - \omega$ range (SET-II), the inclusion of the contribution of core electrons was essential. We adopted the expressions by Eisenberger and Platzman for a bound electron model based on a hydrogenlike atom [41]. In Ref. [41], $S(q, \omega)$ is discussed with/without the impulse approximation (IA), where the electron wave function in the final state is approximated as a plane wave. IA would greatly simplify the problems. Even though this approximation is only valid at the limit of $q \rightarrow \infty$ and $\omega \rightarrow \infty$, the obtained $S(q, \omega)$ reproduces the experiments fairly well in many cases. However, the so-called Raman features, namely the edge feature near the threshold, cannot be implemented. We have adopted the model without IA for a comparison with the experiments.

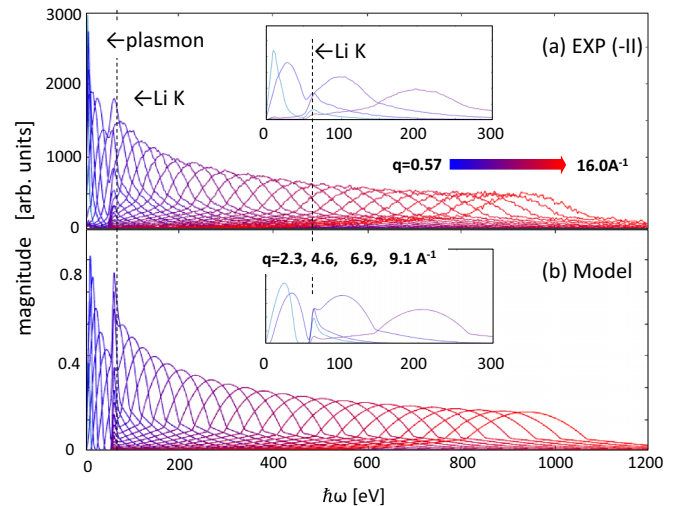


FIG. 1. Experimental (a) and model (b) $S(q, \omega)$. The model is based on RPA implemented with the core contribution.

Li has the most simple core shell and thus the expressions in Ref. [41] are applicable in a straightforward way. The model only consists of a core level and a continuum above a threshold. The final state involves a term of $p^{-1/2} = (2mE_f)^{-1/4}$, where $E_f = \hbar\omega - E_B$, in the normalization prefactor [see Eq. (7) in Ref. [41]] and thus the amplitude of the wave function would display a diverging behavior near the threshold. Nevertheless, this prefactor is canceled out with the density of state of the final state, which is proportional to $E_f^{1/2}$ or p . Here, one can add a small density of states at $E_f = 0$ in order to produce the Raman feature [see Fig. 1(a) in the Supplemental Material [42]]. This procedure is reasonable because the wave function near the threshold should differ from the plane wave in reality and be expressed as the Bloch waves in metals or the localized orbitals in atoms. Note that this is still different from common Raman features because it represents neither band structure in Li metal nor multiplets in a Li atom. However, it is still a good marker to investigate how such an edge feature influences the evolution of the screening charge. After summing $S(q, \omega)_{\text{core}}$ and $S(q, \omega)_{\text{RPA}}$ obtained in the ways mentioned above, we convoluted it with a 5-eV-wide Gaussian for a comparison with the wide range data (SET-II). [See the Supplemental Material [42]; $S(q, \omega)$ and the screening charges due to core electrons with and without IA are compared.]

IV. DERIVATION OF SCREENING CHARGE DENSITY

To obtain the screening charge densities from the dynamical structure factors, we adopt a way similar to ones in other reports [43–45] but somewhat different in details. One defines the potential due to a test charge of $+e$, which is embedded at time $t = 0$,

$$V_{\text{ext}}(r, t) = \frac{e(-e)}{r} \Theta(t). \quad (1)$$

Here, r is the distance from the test charge, $-e$ an electron charge, and $\Theta(t)$ a Heaviside step function, which is 0 for $t < 0$, while 1 for $t \geq 0$. Through Fourier transform (FT) in terms of t , we have

$$\begin{aligned} V_{\text{ext}}(q, \omega) &= \int_{-\infty}^{\infty} dt \int_{-\infty}^{\infty} d^3r V_{\text{ext}}(r, t) e^{-i(\omega t - qr)} \\ &= -\frac{4\pi e^2}{q^2} \left[\pi \delta(\omega) - \frac{1}{i\omega} \right]. \end{aligned} \quad (2)$$

In q - ω space, assuming the homogeneous electron gas model, the induced charge is simply given as [46]

$$\delta n(q, \omega) = V_{\text{ext}}(q, \omega) \chi(q, \omega). \quad (3)$$

To obtain $\delta n(r, t)$, we first perform FT along the ω axis to have $\delta n(q, t)$:

$$\begin{aligned} \delta n(q, t) &= \int_{-\infty}^{\infty} d\omega V_{\text{ext}}(q, \omega) \chi(q, \omega) e^{-i\omega t} \\ &= -\frac{2e^2}{q^2} \{ \pi \text{Re}[\chi(q, 0)] - 2qF(q, t) \}, \end{aligned} \quad (4)$$

where

$$F(q, t) = \int_0^{\infty} d\omega \frac{\text{Im}[\chi(q, \omega)] \cos(\omega t) - \text{Re}[\chi(q, \omega)] \sin(\omega t)}{q\omega}. \quad (5)$$

As the causality is admitted, $\text{Im}[\chi(q, \omega)]$ and $\text{Re}[\chi(q, \omega)]$ satisfy the Kramers-Kronig relationship (see, e.g., Refs. [40,47]). Based on the manner in Refs. [43–45], we have them as follows:

$$\begin{aligned} \text{Im}[\chi(q, \omega)] &= \pi \{ -S(q, -\omega) + S(q, \omega) \}, \\ \text{Re}[\chi(q, \omega)] &= \pi^{-1} P \int_{-\infty}^{\infty} d\omega' \text{Im}[\chi(q, \omega')] (\omega' - \omega)^{-1}, \end{aligned} \quad (6)$$

where P denotes a principal value integral. Finally, we obtain $\delta n(r, t)$ by FT on $\delta n(q, t)$ in three-dimensional q space:

$$\begin{aligned} \delta n(r, t) &= \frac{1}{2\pi^2 r} \int_0^{\infty} dq \delta n(q, t) \sin(qr) \\ &= \frac{e^2}{\pi^2 r} \int_0^{\infty} dq \{ 2F(q, t) - \pi q^{-1} \text{Re}[\chi(q, 0)] \} \sin(qr) \\ &= \frac{2e^2}{\pi^2 r} \int_0^{\infty} dq F(q, t) \sin(qr) + \frac{1}{2} \delta n(r). \end{aligned} \quad (7)$$

Here, the isotropic system is assumed and thus screening occurs as a function of q ($= |\mathbf{q}|$) or r ($= |\mathbf{r}|$). This approach can be applied to an anisotropic system. Then a numerical FT in \mathbf{q} space would be required. The first term in Eq. (7) is dynamic, while the second term static, meaning that the former has time dependence, while the latter does not. In fact, they have the same magnitude with the *opposite* signs when $t = 0$ and thus $\delta n(r, 0) = 0$. When $t \rightarrow \infty$, we find the second term approaches the first term again with the *same* sign. Namely, we just need to make the second term double in order to have the static charge density $\delta n(r, \infty)$. In this paper, the source of the disturbance (here referred to as the test charge) is assumed to be a step function $\Theta(t)$ in Eq. (1), while in the earlier reports a delta function $\delta(t)$ is assumed [43–45,48,49]. Therefore, the expressions have differences but they are basically the same procedure.

V. RESULT AND DISCUSSION

Valence electron screening. Figures 2(a)–2(c) show $-\text{Im}\chi(q, \omega)$, $\delta n(q, t)$, and $\delta n(r, t)$ derived from the high q - ω resolution data (SET-I) along with those for the electron gas model (RPA). In the model, the plasmon shows a quadratic dispersion even for the q range over the critical momentum $q_c = 1 \text{ \AA}^{-1}$: the peak position in ω increases with q increasing across q_c . On the other hand, the experiment indicates the plasmon less dispersive and strongly damped as q increases. The differences between the experiment and the model are also recognizable in $\delta n(q, t)$ [see Fig. 2(b)]. This is an intermediate quantity before obtaining $\delta n(r, t)$, but it provides useful hints to understanding the evolution of the screening charge as a function of time. Since $\delta n(q, t)$ is derived by the Fourier transform of $\text{Im}\chi(q, \omega)$ and corresponding $\text{Re}\chi(q, \omega)$ along the ω axis (or vertical axis), the well defined plasmon peak observed in $\text{Im}\chi(q, \omega)$ leads to the oscillation along the t axis. The plasmon in the model has a long lifetime and shows

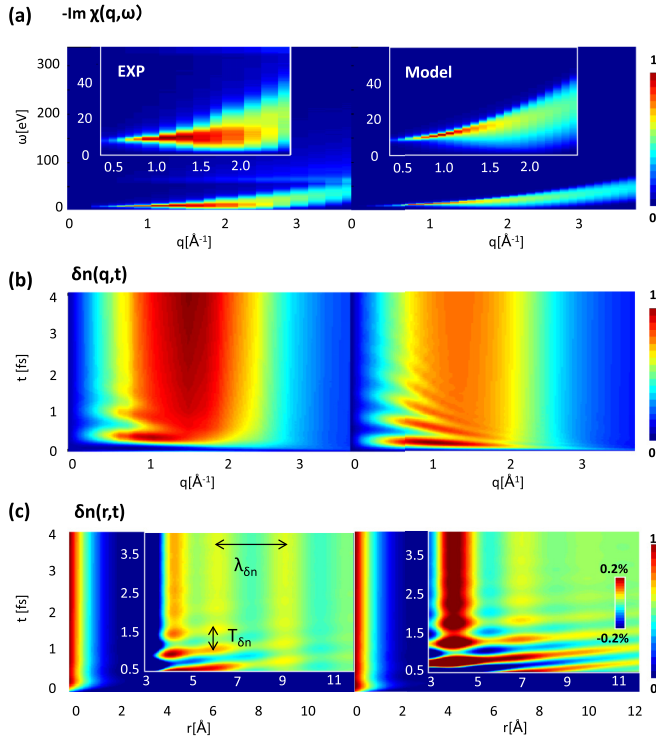


FIG. 2. $-\text{Im}\chi(q, \omega)$ (a), $\delta n(q, t)$ (b), and $\delta n(r, t)$ (c). Left panels indicate those for the experimental data (SET-I), while right panels those for the electron gas model. The theory excludes contributions of core electrons. Note that the color scale in (c) is multiplied by a factor of 400 in the region of $r > 3 \text{ \AA}$ and $t > 0.5 \text{ fs}$.

the oscillation for $t > 2 \text{ fs}$, while it damps at $t \sim 1 \text{ fs}$ in the experiment due to the shorter lifetime.

Finally, $\delta n(r, t)$ is obtained by 3D Fourier transform of $\delta n(q, t)$ along the q (or horizontal) axis [see Fig. 2(c)]. Note the color scales multiplied by a factor of 400 in the region of $r > 3 \text{ \AA}$ and $t > 0.5 \text{ fs}$. The major part of the screening charges is in $r < 3 \text{ \AA}$ around the origin; namely, the charges mostly aggregate around the embedded charge (see also Fig. 4). Nonetheless, an interesting feature is seen in a larger r scale. The stripes appear more and more clearly as t increases, representing the development of the so-called Friedel oscillation. The wave numbers of the stripes are given as $k_{\text{exp}} = 2\pi/\lambda_{\delta n} = 2.14 \text{ \AA}^{-1}$ and $k_{\text{RPA}} = 2.24 \text{ \AA}^{-1}$, which reasonably agree with $2k_F$, where k_F ($= 1.11 \text{ \AA}^{-1}$) is the Fermi wave number obtained from the density of Li. Until the Friedel oscillation fully develops, the screening charge repeats the several beats. The frequencies of the beats are $\omega_{\text{exp}} = 2\pi/T_{\delta n} = 1.2 \times 10^{16} \text{ s}^{-1}$ (at $r = 6.0 \text{ \AA}$ and $t = 1.3 \text{ fs}$), while $\omega_{\text{RPA}} = 1.4 \times 10^{16} \text{ s}^{-1}$ (at 7.0 \AA and 1.1 fs). They correspond to 7.8 eV and 9.2 eV in electron energies, respectively, which are slightly larger than the plasmon energies 7.2 eV (experiment) and 8.2 eV (RPA). The deviations may be ascribed to the plasmon dispersions. The plasmon linewidth $\delta\omega$ is 3.0 eV at $q < 1.0 \text{ \AA}^{-1}$ in the experiment, while that used in RPA is 2.0 eV . The lifetime $\tau = \pi/\delta\omega$ is estimated to be 0.7 fs (experiment) and 1 fs (RPA), which agree well with what we see in Figs. 2(b) and 2(c). The integration of the

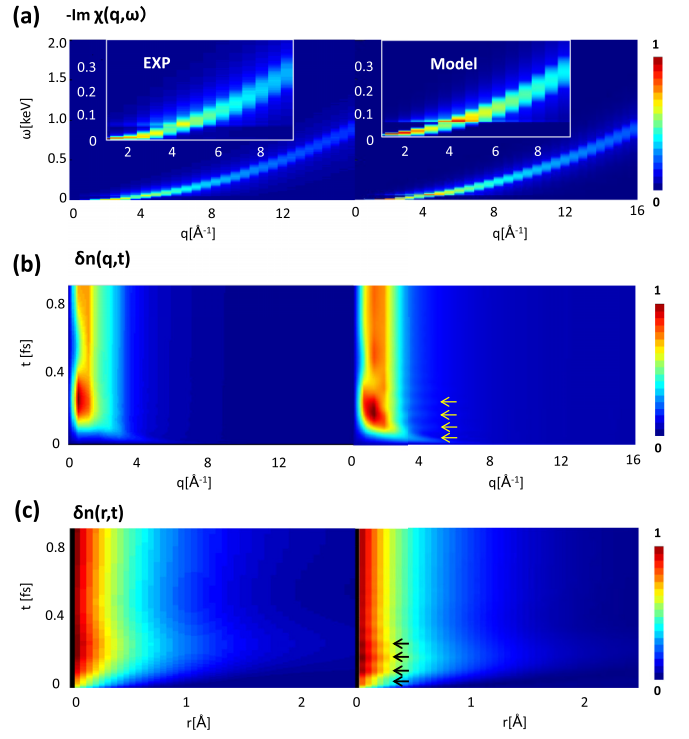


FIG. 3. $-\text{Im}\chi(q, \omega)$ (a), $\delta n(q, t)$ (b), and $\delta n(r, t)$ (c). Left panels indicate those for the experimental data (SET-II), while right panels those for the RPA + coremodel. Arrows show an oscillatory feature due to core electrons.

densities amounts to 0.99 and 1.01 in $r < 5.0 \text{ \AA}$ for the experiment and RPA, respectively.

A prominent difference between the model and the experiment is a phase shift of the oscillation between $r = 4$ and 6 \AA , which is seen in the experiment but not in RPA. The reason is unknown. One possibility is that this is an intrinsic difference between experiment and RPA. The plasmon shows different behaviors in the experiment and RPA as seen in Fig. 2(a) and thus such a phase shift might happen. However, we do not have any other evidence supporting this scenario. Another possibility is the extrinsic effect such as an artifact during the removal of the tail of the elastic scattering. We tried several ways for the subtraction, but such a phase shift still appears. We cannot provide any solid interpretation for this discrepancy.

Core electron screening. Figure 3(a) compares the experimental $-\text{Im}\chi(q, \omega)$ derived from the data set in the wide q - ω range (SET-II) with that from the RPA + coremodel. They appear very similar. A difference is a sharper edge feature near the threshold in the model, which appears more modest in the experiment [see the insets in Fig. 3(a)]. This is because of the model simplified without the band structures in Li metal. It is interesting to see how the edge feature influences the development of the screening charges. Figures 3(b) and 3(c) show the screening charges $\delta n(q, t)$ and $\delta n(r, t)$, respectively. A prominent feature is the fast beats that are seen in the RPA + coremodel (arrows in the right panels). In fact, as seen in Fig. 4, the beats of the same frequency are also discernible in the experiment although they are not as clear as those in the model. The period is commonly

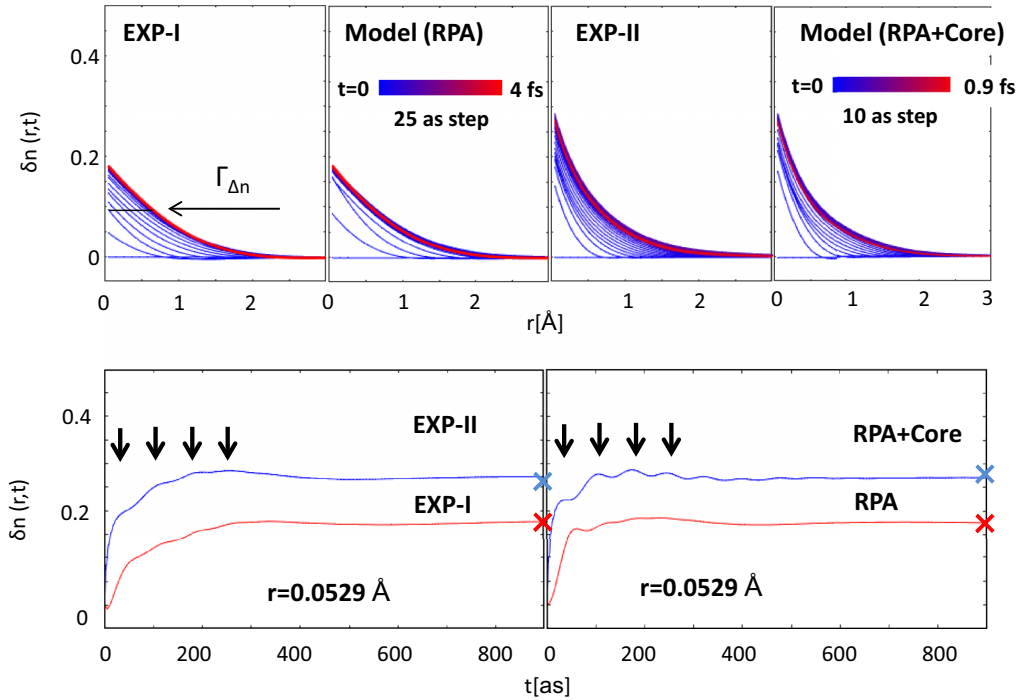


FIG. 4. Upper panels: time slices of screening charge $\delta n(r, t)$ as a function of r . Lower panels: screening charges $\delta n(r, t)$ as a function of t . Here, r stands for the distance from the embedded charge, while t stands for the time duration after the embedding charge. EXP-I means the output from SET-I, while EXP-II that from SET-II. Arrows show an oscillatory feature due to core electrons. Crosses (\times 's) are the charge densities at $t \rightarrow \infty$, which are obtained from $\text{Re}\chi(q, \omega)$.

74 as, which almost coincides with that estimated from the Li K -edge energy, 60 eV, corresponding to 69 as. This oscillatory feature is definitely due to the edge jump at this energy (see the Supplemental Material [42]) [50]. The slightly longer period is due to the contribution from the real part of the $\chi(q, \omega)$ having a spectral weight in the low ω side (not shown). The first beat shows up at $t = 27$ as. This beat makes the trigger for the screening due to the core electrons, which is faster than that due to valence electrons. Note that this oscillation feature is very small in the experiment, although Li has the simplest core level among all the elements. It may be difficult to observe such an oscillation in most of the materials except for the elementary Li and Be metals. Other samples have multiple core levels at larger energies. Generally, deeper core electrons show smaller edge features in an inelastic spectrum.

Compared to the SET-I, where core electron contributions are only partially involved, the SET-II including the full contribution leads to a significantly smaller radius of the induced charge cloud. For example, the half widths at the half maximum of the induced charge cloud $\Gamma_{\Delta n}$ are 0.68 Å and 0.45 Å at $t = 900$ as for the SET-I and the SET-II data, respectively. The former is close to the Thomas-Fermi screening length, 0.61 Å for Li, while the latter is much smaller due to the core electron contribution. Assuming that the potential is uniform at large t , just like a static electric field in metal, a smaller radius of the charge cloud means a smaller effective distance of the potential due to an embedded charge. The model adopted here has a free parameter for the effective nuclear charge Z (see the Supplemental Material [42]), which critically influences the radius of the induced charge cloud, and thus the quantita-

tive comparison may not make a lot of sense ($\Gamma_{\delta n} = 0.66 \text{ \AA}$ for RPA, while 0.40 \AA for RPA + core). Nonetheless it is noted that they consistently indicate that the core electron makes the effective distance for the screening substantially smaller.

An important difference between the experiment and the model is that the screening charge develops more slowly in the experiment. This tendency is more clearly recognized in the valence electron screening (cf. EXP-I and RPA in Fig. 4). The first beat shows up at 50 as and this reaches more than 90% of the static screening charge in magnitude. In the experiment, the charge develops more slowly and shows the maximum at 200–300 as. This is ascribed to the different dispersions of the plasmon peaks. The plasmon peak at $\omega = 8.2 \text{ eV}$ in RPA has a large dispersion. The peak shifts to the higher ω side as q increases, meaning that fast components are involved for the screening. In contrast, the plasmon peak at 7.2 eV observed in experiment only shows a very small dispersion. The difference suggests the electron correlation effect and/or the orbital hybridization between the valence and core electrons impedes the development of the fast response and slows down the aggregation of the screening charges.

VI. CONCLUSION

When a test charge is embedded in a metal, a screening due to core electrons first occurs, and then it is followed by the screening due to the valence electrons. The screening by the valence electrons displays an oscillatory feature with a frequency (of penta-Hz) corresponding to the plasmon energy

(of ~ 10 eV), finally leading to a static screening charge in femtoseconds. The static screening charge consists of an electron cloud surrounding the embedded charge within several Å and the Friedel oscillation in a larger r scale. The core electrons form fast and local screening charges and they contribute to making the effective distance for the potential smaller. The core electrons having a binding energy of ≥ 100 eV (in general) display the oscillatory behavior with a frequency of ≥ 10 penta-Hz, determined by the absorption edge energy. Compared to those in the electron gas model, the experimentally observed screening charges slowly develop. This suggests that the electron correlation effect and/or the orbital

hybridization impedes the fast response and slows down the charge aggregation.

ACKNOWLEDGMENTS

We thank A. Yamamoto for his help with the sample preparation. The experiments were performed under approvals of Japan Synchrotron Radiation Research Institute (JASRI), SPring-8 (Proposals No. 2018A4261, No. 2018B4260, and No. 2020A4251) and National Synchrotron Radiation Research Center (NSRRC), Taiwan (Proposals No. 2018-2-189, No. 2018-3-180, and No. 2020-1-298).

-
- [1] C. A. Ullrich, *Time-Dependent Density-Functional Theory: Concepts and Applications* (Oxford University Press, Oxford, 2011).
- [2] L. Reining, V. Olevano, A. Rubio, and G. Onida, *Phys. Rev. Lett.* **88**, 066404 (2002).
- [3] S. Botti, *Phys. Scr.* **T109**, 54 (2004).
- [4] J. Sun, C.-W. Lee, A. Kononov, A. Schleife, and C. A. Ullrich, *Phys. Rev. Lett.* **127**, 077401 (2021).
- [5] R. M. Martin, L. Reining, and D. M. Ceperley, *Interacting Electrons: Theory and Computational Approaches* (Cambridge University Press, Cambridge, UK, 2016).
- [6] C. A. Kukkonen and K. Chen, *Phys. Rev. B* **104**, 195142 (2021).
- [7] S. Azadi and N. D. Drummond, *Phys. Rev. B* **105**, 245135 (2022).
- [8] G. D. Mahan, *Many-Particle Physics* (Kluwer Academic/Plenum, New York, 2000).
- [9] G. Giuliani and G. Vignale, *Quantum Theory of the Electron Liquid* (Cambridge University Press, Cambridge, UK, 2005).
- [10] L. G. Stanton and M. S. Murillo, *Phys. Rev. E* **91**, 033104 (2015).
- [11] Y. Takada, *Eur. Phys. J. B* **91**, 189 (2018).
- [12] T. J. Sjöstrand, F. Nilsson, C. Friedrich, and F. Aryasetiawan, *Phys. Rev. B* **99**, 195136 (2019).
- [13] Y. Pavlyukh, G. Stefanucci, and R. van Leeuwen, *Phys. Rev. B* **102**, 045121 (2020).
- [14] S. Ahn and S. Das Sarma, *Phys. Rev. B* **103**, 165303 (2021).
- [15] B. Chatterjee, J. Skolimowski, and K. Byczuk, *Phys. Rev. B* **105**, 235129 (2022).
- [16] T. Dornheim, J. Vorberger, and M. Bonitz, *Phys. Rev. Lett.* **125**, 085001 (2020).
- [17] T. Dornheim, M. Böhme, Z. A. Moldabekov, J. Vorberger, and M. Bonitz, *Phys. Rev. Res.* **3**, 033231 (2021).
- [18] M. F. Crommie, C. P. Lutz, and D. M. Eigler, *Nature (London)* **363**, 524 (1993).
- [19] Y. Hasegawa and P. Avouris, *Phys. Rev. Lett.* **71**, 1071 (1993).
- [20] P. T. Sprunger, L. Petersen, E. W. Plummer, E. Lægsgaard, and F. Besenbacher, *Science* **275**, 1764 (1997).
- [21] X. Chen, W. Duan, X. Fan, W. Hong, K. Chen, H. Yang, S. Li, H. Luo, and H.-H. Wen, *Phys. Rev. Lett.* **126**, 257002 (2021).
- [22] M. D. Johnson and N. H. March, *Phys. Lett.* **3**, 313 (1963).
- [23] J.-P. Hansen and I. R. McDonald, *Theory of Simple Liquids*, 3rd ed. (Academic Press, New York, 2005).
- [24] J. J. Kas, F. D. Vila, J. J. Rehr, and S. A. Chambers, *Phys. Rev. B* **91**, 121112(R) (2015).
- [25] J. C. Woicik, C. Weiland, A. K. Rumaiz, M. T. Brumbach, J. M. Ablett, E. L. Shirley, J. J. Kas, and J. J. Rehr, *Phys. Rev. B* **101**, 245105 (2020).
- [26] C. A. Schmuttenmaer, M. Aeschlimann, H. E. Elsayed-Ali, R. J. D. Miller, D. A. Mantell, J. Cao, and Y. Gao, *Phys. Rev. B* **50**, 8957(R) (1994).
- [27] T. Hertel, E. Knoesel, M. Wolf, and G. Ertl, *Phys. Rev. Lett.* **76**, 535 (1996).
- [28] M. Aeschlimann, M. Bauer, S. Pawlik, W. Weber, R. Burgermeister, D. Oberli, and H. C. Siegmann, *Phys. Rev. Lett.* **79**, 5158 (1997).
- [29] A. L. Cavalieri, N. Müller, T. Uphues, V. S. Yakovlev, A. Baltuška, B. Horvath, B. Schmidt, L. Blümel, R. Holzwarth, S. Hendel *et al.*, *Nature (London)* **449**, 1029 (2007).
- [30] S. Hellmann, T. Rohwer, M. Källäne, K. Hanff, C. Sohr, A. Stange, A. Carr, M. M. Murnane, H. C. Kapteyn, L. Kipp *et al.*, *Nat. Commun.* **3**, 1069 (2012).
- [31] K. Klünder, J. M. Dahlström, M. Gisselbrecht, T. Fordell, M. Swoboda, D. Guénot, P. Johnsson, J. Caillat, J. Mauritsson, A. Maquet *et al.*, *Phys. Rev. Lett.* **106**, 143002 (2011).
- [32] C. Chen, Z. Tao, A. Carr, P. Matyba, T. Szilvási, S. Emmerich, M. Piecuch, M. Keller, D. Zusin, S. Eich *et al.*, *Proc. Natl. Acad. Sci. USA* **114**, 5300 (2017).
- [33] T. Hagiya, K. Matsuda, N. Hiraoka, Y. Kajihara, K. Kimura, and M. Inui, *Phys. Rev. B* **102**, 054208 (2020).
- [34] W. Schülke, H. Nagasawa, and S. Mourikis, *Phys. Rev. Lett.* **52**, 2065 (1984).
- [35] W. Schülke, H. Nagasawa, S. Mourikis, and P. Lanzki, *Phys. Rev. B* **33**, 6744 (1986).
- [36] J. P. Hill, C. C. Kao, W. A. C. Caliebe, D. Gibbs, and J. B. Hastings, *Phys. Rev. Lett.* **77**, 3665 (1996).
- [37] N. Hiraoka, H. Fukui, H. Tanida, H. Toyokawa, Y. Q. Cai, and K.-D. Tsuei, *J. Synchrotron Rad.* **20**, 266 (2013).
- [38] N. Hiraoka, Y. Yang, T. Hagiya, A. Niozu, K. Matsuda, S. Huotari, M. Holzmann, and D. M. Ceperley, *Phys. Rev. B* **101**, 165124 (2020).
- [39] Y. Yang, N. Hiraoka, K. Matsuda, M. Holzmann, and D. M. Ceperley, *Phys. Rev. B* **101**, 165125 (2020).
- [40] M. Dressel and G. Grüner, *Electrodynamics of Solids* (Cambridge University Press, Cambridge, UK, 2002), Chap. 4.
- [41] P. Eisenberger and P. M. Platzman, *Phys. Rev. A* **2**, 415 (1970).

- [42] See Supplemental Material at <http://link.aps.org/supplemental/10.1103/PhysRevB.108.195104> for the details of the derivation of the screening charge and the models with/without the impulse approximation.
- [43] P. Abbamonte, K. D. Finkelstein, M. D. Collins, and S. M. Gruner, *Phys. Rev. Lett.* **92**, 237401 (2004).
- [44] P. Abbamonte, J. P. Reed, Y. I. Joe, Y. Gan, and D. Casa, *Phys. Rev. B* **80**, 054302 (2009).
- [45] P. Abbamonte, G. Wong, D. G. Gahill, J. P. Reed, R. H. Coridan, N. W. Schmidt, G. H. Lai, Y. I. Joe, and D. Casa, *Adv. Mater.* **22**, 1141 (2010).
- [46] K. Sturm, *Z. Naturforsch* **48**, 233 (1993).
- [47] W. Schülke, *Electron Dynamics by Inelastic X-ray Scattering* (Oxford University Press, Oxford, 2007), Chap. 4.
- [48] R. H. Coridan, N. W. Schmidt, G. H. Lai, R. Godawat, M. Krisch, S. Garde, P. Abbamonte, and G. C. L. Wong, *Phys. Rev. Lett.* **103**, 237402 (2009).
- [49] J. P. Reed, B. Uchoa, Y. I. Joe, Y. Gan, D. Casa, E. Fradkin, and P. Abbamonte, *Science* **330**, 805 (2010).
- [50] The RPA without the core model also shows a weak oscillation appearing somewhat similar, but the period is 59 as, which is significantly smaller from the ones observed in EXP-II.